

Pushbroom imaging spectrometer design for optimum recovery of spectroscopic and spatial information

Pantazis Mouroulis, Robert O. Green, Thomas G. Chrien
Jet Propulsion Laboratory
California Institute of Technology
Pasadena, CA 91109

Abstract

An MTF-based optimization method is described that can extract maximum spectral and spatial uniformity of response from compact pushbroom imaging spectrometer designs. Such uniformity is essential in extracting accurate spectroscopic information from a pushbroom sensor in Earth-observing remote sensing applications. Two simple and compact spectrometer design examples are described that can satisfy stringent uniformity specifications.

1. Introduction

There is increasing interest in remote sensing of the Earth from space for monitoring of natural resources, mineral exploration, hazard remediation, and several other applications. Hyperspectral imaging spectroscopy¹ is one of the main means of filling that need, and pushbroom sensors offer the signal-to-noise performance that is required for orbiting platforms. However, such sensors do not easily yield high quality spectroscopic data. This means that the recovered spectrum of any ground feature from a pushbroom sensor can potentially contain substantial artifacts that compromise identification of its chemical composition. Further, pushbroom spectrometer artifacts can cause pixel classification algorithms to fail by producing many non-physical spectral signatures.

The detailed justification of how these errors arise as well as their effects on the recovery of information from remotely sensed data is beyond the scope of this paper, but has been given in refs. (2,3). Here we concentrate on how the spectrometer optical design can help alleviate the errors.

2. Sources of data artifacts in pushbroom imaging spectrometers

It is instructive to consider first a whiskbroom sensor, since this type can achieve the highest theoretical data quality in principle. Whiskbroom sensors are more appropriate for airborne rather than orbiting platforms, since they cannot easily provide adequate signal-to-noise performance from orbit due to the limited integration time. However, a whiskbroom sensor records the spectrum of every point on the ground on a single linear photodetector array. Hence careful calibration of the response of each individual detector element suffices to eliminate most artifacts. This process has been tested in practice, using what is perhaps the single most successful hyperspectral imaging spectrometer, AVIRIS^{4,5} which is operated from various airplane platforms.

Consider first the spectral calibration procedure. For a whiskbroom sensor such as AVIRIS, it consists of accurate measurement of the spectral response function (SRF) of each pixel.⁶ For AVIRIS, it has been determined experimentally that the SRF of all pixels is closely approximated by a Gaussian, and can thus be characterized by the location of its maximum and its halfwidth (full width at half-maximum). These two parameters must be known very accurately; an estimate of 1% error in the center location and 2% error in the halfwidth have been identified as desirable for producing data substantially free from spectral artifacts.³

Consider now a pushbroom sensor. The slit is dispersed and imaged on an area array, the columns of which are considered here parallel to the slit, with the rows thus providing the spectral information. Each row is effectively an independent spectrometer. Thus if a pushbroom sensor is to produce data of the same quality as a whiskbroom one, the SRF of every pixel must be calibrated to the same 1-2% accuracy mentioned

above. That of course is not practical, as it would multiply the already demanding whiskbroom calibration procedure by the number of spatial pixels (typically several hundred). But even if it were somehow possible to perform the above calibration, there would still be a problem with the recovery of the information, since a correction algorithm would have to be applied to every pixel, thus increasing computational complexity beyond reasonable limits. It is therefore desirable to have the same spectral calibration for all rows of the array.

There are, however, additional problems with pushbroom systems that relate to the spatial direction. These have mostly to do with spatial uniformity and cross-contamination of the spectra between adjacent spatial pixels. It is easiest to appreciate these errors with the help of a pictorial representation. Figure 1 shows the ideal spectrum that a pushbroom imaging spectrometer must produce. The columns labeled “B”, “G”, and “R” represent the short, middle, and long wavelength images of the slit respectively. The filled circles or ellipses represent idealized optical point spread functions (PSFs).

The following desirable optical characteristics are evident from the figure. All spectra are perfectly parallel between them and with the rows of the array. Similarly, the monochromatic slit image for any wavelength is perfectly straight and aligned with a column. In other words, the centroids of the PSFs form a perfect rectangle. This means that distortion in both the spectral and spatial directions must be absent. Further, the width of the PSF (a or b) along any column also remains constant, though it is allowed to vary with wavelength. Finally, the height of the PSF (indicated by c) should remain constant, independent of wavelength, and also independent of spatial location.

In practice, these conditions can only be satisfied approximately. A non-ideal spectrum that contains all possible errors is shown in Fig. 2. The figure shows the following errors.

- The “B” column exhibits a distortion that is called “smile”. This error will affect knowledge of the location of the peak of the SRF of a pixel.
- The “G” column shows variation in the width of the PSF with spatial location. This error will affect knowledge of the halfwidth or shape of the spectral response function.
- The top row is not aligned with the array, and when compared with the middle one, it shows that the spectrum is more like a trapezoid than a rectangle. This is called “keystone error”; it causes contamination of spectra from adjacent pixels in boundary regions or for objects that are only a few pixels wide.
- The bottom row shows a PSF that increases in height with wavelength (as might be caused by diffraction). Although this may be inevitable in a diffraction-limited system, it nevertheless causes a spatial nonuniformity similar to the keystone error.

The tolerance for all the above errors is at the level of a small fraction of a pixel. The desirable level of control for the first two errors is $< \sim 2\%$ and for the last two $< \sim 5\%$ of a pixel.³

It is evident that these requirements are rather demanding. However, the recovered data quality will depend on the extent to which they are satisfied. Hence a pushbroom imaging spectrometer design procedure should take them into account. This should be done preferably at the optimization stage, and some merit function recommendations are provided within this paper. But in any case, the performance assessment of a design in terms of the above errors should be an integral part of imaging spectrometer design evaluation, as shown in the following sections.

3. Computation and optimization of optical requirements

This section shows how the requirements put forth in Sec. 2 can be computed and translated into terms appropriate for incorporation into a merit function.

3.1. Smile and keystone

Minimization of smile and keystone is the simplest requirement to quantify and insert into the merit function. The chief rays from two or three points in the field are selected for three wavelengths spanning

the desired spectral range. The intersections of these rays with the image plane are noted and their differences in x or y coordinates are then set to zero with an appropriate weighting factor. In order to calculate the exact amount of smile or keystone one must consider not the chief ray intersections but the PSF centroid locations. There is, in general, a difference between the two, which however diminishes as the level of distortion and aberration decreases. The chief ray intersection is computed much faster than the centroid which requires many rays and its use has been found perfectly adequate in reducing smile and keystone (as computed through the centroids) to practically undetectable levels.⁷

A slight wrinkle to the above procedure appears when the PSF is strongly asymmetric, leading to an asymmetric SRF. In that case, the SRF cannot be described through the peak value (or mode) and halfwidth (or variance) alone. Additional moments may be needed (median, skewness, etc.). If, in other words, the SRF changes shape considerably as a function of the field position by becoming asymmetric, the definition of smile becomes problematic. For the functions of interest, the location of the centroid of the PSF still predicts the median (but not mode) value of the SRF. In any case, by reducing the SRF variation with field position, as in the following section, this concern is mitigated.

3.2. SRF variation with field position

The SRF is the convolution of the slit image with the pixel response function, where the latter is simply assumed to be a rect function. This assumption may not be correct,⁸ but in the absence of detailed information it provides a starting point. The slit image is itself a convolution of the slit (a rect function) and the optical line spread function (LSF) in the tangential direction. Typically, the slit is of the same width as the pixel, say y_0 . Thus we have

$$\text{SRF} = \text{rect}(y_0) \otimes \text{LSF}_T \otimes \text{rect}(y_0) \quad (1)$$

where \otimes denotes convolution. If LSF_T is narrow compared to the pixel or slit width then the SRF resembles a triangle function of halfwidth $\sim y_0$. Otherwise, if the LSF size is comparable to the pixel, the SRF begins to resemble a Gaussian with a halfwidth broader than y_0 .

In practice, the SRF is measured by illuminating the spectrometer with monochromatic light and varying the wavelength while recording the output of the pixel under test. The image of the slit thus shifts along the pixel, giving a function that peaks when the middle of the slit image coincides with the middle of the pixel. In order to represent this experimental procedure by Eq. (1), the assumption must be made that the LSF is approximately independent of wavelength, an assumption that can be taken as valid over the restricted wavelength range that excites any one pixel. However, globally the LSF is a non-trivial function of wavelength.

In the Fourier domain, the convolutions become multiplications. The Fourier transform of the SRF may be thought of as a form of spectral MTF,⁹ and hence is denoted as SMTF. Thus (1) becomes

$$\text{SMTF} = \text{MTF}_T \cdot \text{sinc}^2(1/y_0) \quad (2)$$

where MTF_T the tangential MTF of the spectrometer, defined here to coincide with the (spatial) MTF along the spectral direction. Equation (1) is used in order to compute the SRF for design evaluation purposes. However, Eq. (1) is not suited for use during design optimization, as the computations inherent in it would slow down the optimization considerably. Specifically, an operand relating to the extent (or integrated energy) of the LSF would have to be devised (spot or ray-based operands are a poor substitute for near diffraction-limited systems). If the optical design software offers such an operand, it may be advantageous to use it. But it is more likely that one will have to resort to Eq. (2), which shows that we can use MTF-based operands, offered by practically every advanced design program. Specifically, we can demand that the tangential MTF remains approximately constant independent of field position, for a spatial frequency up to $1/y_0$ that defines the first zero of the sinc^2 function.

3.3. PSF variation with wavelength

The last constraint expressed in figures 1, 2 is the minimization of the variation of the PSF height as a function of wavelength, which provides a uniform spatial response function. The spatial response function (SiRF) along the spatial direction (length of slit) is simply the convolution of the pixel with the sagittal LSF.

$$\text{SiRF} = \text{rect}(x_0) \otimes \text{LSF}_S \quad (3)$$

In the Fourier domain, the spatial response function becomes the spectrometer spatial transfer function (SSTF). So (3) is written as

$$\text{SSTF} = \text{MTF}_S \cdot \text{sinc}(1/x_0) \quad (4)$$

showing again that we can use the MTF up to a fixed frequency for optimization purposes. It should be appreciated that the ideal spectrum shown in Fig. 1 applies to imaging from orbit. The wavelength-dependent scattering of the atmosphere modifies the SiRF or SSTF. Generally, the 'blue' end will suffer from more scattering and hence broadening of the LSF. This means that even if one measures the ideal spectrum of Fig. 1 during ground calibration, the spectrometer will behave differently once in orbit. Conceptually, the inclusion of the atmospheric effect provides no difficulty. We can simply multiply the right hand side of (4) by the atmospheric MTF.

$$\text{SSTF} = \text{MTF}_A \cdot \text{MTF}_S \cdot \text{sinc}(1/x_0) \quad (5)$$

In practice, MTF_A is variable and can only be predicted within broad limits, which means that one can only optimize to a mean expected response. Atmospheric MTF measurements have been performed at ground level,¹⁰ but we know of no measurements of the down-looking atmospheric MTF through the range of wavelengths that is of interest here. If, however, such measurements become available they can be incorporated in the design procedure through Eq. (5).

The effect of the atmosphere is more critical at short wavelengths. In the solar reflected portion of the spectrum the interaction between upwelling radiance and the atmosphere takes the form of absorption and scattering. Water vapor, carbon dioxide, oxygen, methane, and ozone are the primary molecules that absorb solar energy in the atmosphere. Both the molecules and aerosols of the atmosphere are responsible for scattering radiance. The upwelling spectral radiance reaching an imaging spectrometer can be separated into two primary components: (1) the energy that has been reflected by the surface, (2) and the energy that has been scattered by the atmosphere into the observation direction of the sensor. Figure 3 shows the relative contribution of these two components. It can be seen that the proportion of scattered energy decreases from 400 nm to 1000 nm, and is negligible thereafter. The scattered energy has the effect of broadening the spatial response function, but the main problem is not the broadening by itself, but the wavelength dependence of the effect, which affects the spatial response uniformity.

It is noted here that the atmospheric MTF will affect the response function in the spectral direction (and thus on the SRF) as well as the spatial direction. This is generally not a problem since one can expect that it will have a similar effect on all SRF's. However, this assumption may be violated in systems with a very wide field of view, in which case the atmospheric effect may vary as a function of field position.

Minimizing the change in SiRF with wavelength is equivalent to minimizing the sagittal LSF variation, and may be expressed as

$$\text{LSF}_S(\lambda_1) = \text{LSF}_S(\lambda_2) , \quad \forall \lambda_1, \lambda_2 \quad (6)$$

It is fortunate that physics works in our favor here, since at the short wavelength end the LSF (or PSF) tends to be degraded by aberrations, while at the long wavelength end diffraction is typically dominant. Thus one has to seek a balance between these two effects. In practice, this may mean that we accept worse image quality at the short wavelength end than the spectrometer is capable of providing, but the reduction

in image quality is more than balanced by the improvement in the spatial/spectral uniformity. Equation (6) should be understood as applying to the LSF from orbit and thus containing the effects of the atmosphere as well.

Condition (6) is in fact physically impossible to satisfy in that strict form. However, we can approximate that condition by following the reasoning of the previous section and using MTF-based operands in the merit function. Thus we attempt to equalize the two MTFs up to the frequency $1/x_0$. From Eq. (5),

$$\text{MTF}_A(\lambda_1, f_i) \cdot \text{MTF}_S(\lambda_1, f_i) = \text{MTF}_A(\lambda_2, f_i) \cdot \text{MTF}_S(\lambda_2, f_i) \quad (7)$$

where f_i can be taken as two spatial frequencies, $1/x_0$ and $1/2x_0$. Equation (7) is empirical, rather than strict. Limiting the integral over one pixel (or the MTF up to the frequency $1/x_0$) is somewhat arbitrary, but it suffices in practice to ensure that the undesired variation is minimized. If the atmospheric MTF cannot be estimated in a satisfactory way, one may at least partly account for it by assigning weak weighting factors in the merit function operands relating to Eq. (7). This will generally result in a LSF that increases slightly with wavelength. Equation 7 needs to be applied to several different field positions. In practice, it has been found sufficient to use three appropriately selected field positions.

As explained earlier, the effect of the atmosphere becomes negligible for wavelengths longer than about 1000 nm, in which case we can take $\text{MTF}_A(\lambda_1, f_i) = \text{MTF}_A(\lambda_2, f_i)$ in Eq. 7. However, the method of optimization shown here is independent of that assumption, which in any case does not hold for shorter wavelengths. If the atmospheric effect is strongly nonlinear with wavelength (e.g. Rayleigh scattering) then using two wavelengths only, as implied by Eq. 7, is in principle inadequate. Three wavelengths would suffice to represent even strongly nonlinear cases. However, in practice it is probably adequate to use two wavelengths only, since the optical design will be able to satisfy any condition similar to (7) only approximately. In any case, the evaluation of the resulting design can always show if a satisfactory solution has been obtained.

There remains one requirement that has not been addressed yet: that the height of the PSF ('c' in Fig. 1) remains constant, independent of field. If that condition can be satisfied, then the spectrometer will have the maximum degree of spatial uniformity. However, the condition is difficult to quantify since the height c is not completely independent of wavelength. In the optimization method adopted here, this condition is not evaluated explicitly, but it has been found in practice that the residual variation with field of the PSF height is similar in magnitude to the residual variation with wavelength, when an attempt has been made to reduce the latter.

The optical design may lack enough degrees of freedom to satisfy all conditions described in sections 3.1-3.3. Nevertheless, by inserting the conditions into the merit function one may seek an appropriate balance between them. We may also note that the significance of the keystone error and of the LSF variation with wavelength is lessened if a relatively unstructured field is imaged. An example of such an application is ocean monitoring. In that case, minimization of smile and of the SRF variation should be the prime goals of the design. However, for typical land applications sharp borders and small targets are common, in which case all the above conditions need be considered.

4. Optical design examples

Progress in spectrometer design has resulted in the development of concentric spectrometer forms, which are noted for their simplicity and compactness. These forms achieve their desirable characteristics by placing the grating on a spherical surface within a nominally concentric reflecting or catadioptric system.¹¹⁻¹⁷ They also can achieve very low distortion values because of their symmetric form.¹⁸ The full potential of these spectrometers is now being tapped thanks to recent improvements in techniques for manufacturing high-quality blazed gratings on the curved surface.¹⁹ Within the context of this work, we undertook to evaluate concentric spectrometer forms for their ability to satisfy all the requirements for spatial and spectral uniformity described in the previous sections.

These designs have only a limited number of degrees of freedom. As it will be seen, however, they can be made to satisfy stringent requirements while employing only two spherical surfaces. In practice, one trades a little image quality to gain uniformity of response. This trade is demonstrated by comparing between two versions of the same spectrometer: one that has been optimized for distortion and image quality only, and one that has been optimized for uniformity of response in addition to distortion and image quality. For the examples shown below, we have specifically chosen not to increase the number of optimization variables even as we impose additional requirements for uniformity. Of course, depending on the specifications of a specific desired system, one may have to use additional variables such as aspherizing or tilting various surfaces, employing some aberration correction or balancing in the grating, and so on. None of these variables were used here. The designs have only spherical surfaces with a common axis.

For brevity, a spectrometer covering the 1000-2500 nm range is presented only. Normally, another module covering the 400-1000 nm range would also be required in order to cover the entire spectral range of interest in typical Earth-looking hyperspectral remote sensing applications. Our aim is to demonstrate the application of the method rather than produce final designs. For this reason we can also ignore any effects arising from the front light collection optics, since the actual optical system is transparent to the optimization method (in practice of course, the front optic cannot be ignored insofar as it may cause a non-uniform change of the PSF with field or wavelength). Similarly, atmospheric effects can be included once a reliable mean atmospheric MTF is known without any changes in the method but only perhaps in the weighting factors assigned to the various merit function operands.

The first example is an Offner spectrometer, shown in Fig. 4. This spectrometer has a nominal resolution of 10 nm (150 spectral pixels), and 720 spatial pixels of 27 μm square size. The f-number is 4. The two differently optimized versions of the spectrometer look identical at this level of accuracy. Both versions have negligible smile (<1%) and keystone (<2%). The ensquared energy in the pixel is >79% for both spectrometers and at all field positions and wavelengths. The spectrometer optimized for uniform response (hereafter called "Offner 2") has a lower overall image quality at all wavelengths compared with the spectrometer optimized primarily for distortion ("Offner 1"). The Strehl ratio for Offner 2 is ~ 0.72 at the long wavelength end whereas Offner 1 has a Strehl of ~ 0.8 . At the short wavelength end, the Strehl for Offner 1 varies from 0.56 to 0.99, whereas for Offner 2 the Strehl varies from 0.16 to 0.35.

Figure 5 shows the maximum SRF variation for Offner 1, and Fig. 6 the maximum SRF variation for Offner 2. It can be seen that the method succeeded in reducing further the SRF variation while not causing a significant broadening of the response (halfwidth). A similar though more pronounced improvement can be seen in the variation of the SiRF for the two spectrometers, shown in figures 7, 8. We defer a more detailed discussion of the differences between the various curves of Figs. 5-8 until the next example.

The second example is a Dyson spectrometer, shown in Fig. 9 in schematic form. This spectrometer also has a nominal resolution of 10 nm, but has a larger number of spatial pixels (1000) of 18 μm square size, and an f-number of 1.4. The two differently optimized versions of the spectrometer look very similar, with the second having a slightly larger air gap ($\sim 10\%$) between lens and grating. The first version, called "Dyson 1", was optimized for distortion and image quality. It has negligible levels of smile and keystone (<1%), and > 78% spot energy inside the pixel for all wavelengths and field positions. However, the spectral and spatial response function variation is considerable. For the SRF, (Fig. 10), the difference in halfwidth between the two curves is estimated to be around 8%. The difference in shape between the two curves makes it difficult to quantify the overall effect of their differences on the accuracy of the recovered spectra. But for the sake of this example, we may accept that the overall difference between the two curves can be sufficiently characterized by the difference in their halfwidth alone. Under that assumption, we would be able to accept as much as 4% smile before it became the dominant source of error. Thus the high level of smile correction achieved in the design is partly negated by the SRF variation. A more balanced design would have allowed some smile in exchange for SRF variation reduction.

Similar considerations apply for keystone and the SiRF variation, shown in Fig. 11. Again, the SiRF variation is considerable. If we characterize this variation by the integral of the SiRF outside the main pixel, (corresponding to the intervals 0-1 and 2-3 in the abscissa of Fig. 11, we see that this integral is approximately 13% (diamonds) and 28% (squares) of the total integral. The net variation (difference)

therefore is 15%. There is no simple way to convert this variation to an equivalent keystone error, but we may take it to be approximately equivalent to $\frac{1}{2}$ that value (i.e., 7-8%) in keystone, since the keystone error is unidirectional, whereas the SiRF variation is similar in both directions. Thus again, although this level of equivalent keystone is not very high and may indeed be tolerable in a good system, it still demonstrates that correcting keystone to less than 1% was unnecessary, and that the performance of the system will not be limited by keystone but by the SiRF variation.

The second version of the Dyson spectrometer ("Dyson 2") was optimized for optimum uniformity of response. It has smile of < 2% and keystone of < 1%. The energy ensquared in the pixel for all fields and wavelengths is >84%. The uniformity of response is basically achieved by broadening the spots at the short wavelength end, but not excessively. The SRF variation for this spectrometer is shown in Fig. 12. It can be seen that this is a rather small variation, consistent with the level of smile of 2%. The SiRF variation is shown in Fig. 13. Following the rationale of the previous paragraph, the equivalent keystone error caused by the SiRF variation is now only about 3%, which is consistent with high quality data extraction.

5. Conclusions

This work has demonstrated means for optimally balancing a spectrometer design in terms of image quality, spectral and spatial distortion, and spectral and spatial response function variation. It has been shown that an optimization method based on the MTF can provide the needed uniformity of response. Two examples of realistic spectrometer systems have been shown, which demonstrate that tight specifications can be achieved with simple spectrometer designs possessing only few degrees of freedom.

This research was performed at the Jet Propulsion Laboratory, California Institute of Technology, under a contract with the National Aeronautics and Space Administration.

References

1. See for example SPIE Proc. vol. 3438, *Imaging Spectrometry IV*, M. R. Descour and S. S. Shen Eds, (1998) and previous volumes of the same conference series.
2. R. O. Green: "Spectral calibration requirement for Earth-looking imaging spectrometers in the solar-reflected spectrum", *Appl. Opt.* **37**, 683-690 (1998)
3. P. Mouroulis, D. A. Thomas, T. G. Chrien, V. Duval, R. O. Green, J. J. Simmonds, and A. H. Vaughan: "Trade studies in multi/hyperspectral imaging systems: Final Report" NASA Internal Report, available at <http://ntrpio.nasa.gov/esto.html> (1998)
4. G. Vane, M. Chrisp, H. Enmark, S. Macenka, and J. Solomon: "Airborne Visible/Infrared Imaging Spectrometer: An advanced tool for Earth remote sensing", *Proc. 1984 IEEE Intl. Geoscience and Remote Sensing Symposium*, vol. SP 215, 751-757 (1984).
5. R. O. Green, M. L. Eastwood, C. M. Sarture, T. G. Chrien, M. Aronsson, B. J. Chippendale, J. A. Faust, B. E. Pavri, C. J. Chovit, M. Solis, M. R. Olah, and O. Williams: "Imaging spectroscopy and the Airborne Visible/Infrared Imaging Spectrometer (AVIRIS)", *Remote Sens. Environ.* **65**, 227-248 (1998)
6. T. G. Chrien, R. O. Green, and M. L. Eastwood: "Accuracy of the spectral and radiometric laboratory calibration of the Airborne Visible/Infrared Imaging Spectrometer (AVIRIS)", in *Imaging Spectroscopy of the Terrestrial Environment*, SPIE Proc. **1298**, 37-49 (1990)
7. P. Mouroulis: "Low-distortion imaging spectrometer designs utilizing convex gratings", in *International Optical Design Conference 1998*, L. R. Gardner and K. P. Thompson Eds., SPIE Proc. **3842**, 594-601 (1998)
8. D. Kavaldjiev and Z. Ninkov: "Subpixel sensitivity map for a charge-coupled device sensor", *Opt. Eng.* **37**, 948-954 (1998)
9. D. R. Hearn: "Characterization of instrument spectral resolution by the spectral modulation transfer function" in *Earth Observing Systems III*, W. L. Barnes Ed., SPIE Proc. **3439**, 400 - 407 (1998)
10. I. Dror and N. S. Kopeika: "Experimental comparison of turbulence modulation transfer function and aerosol modulation transfer function through the open atmosphere", *J. Opt. Soc. Am. A* **12**, 970-980 (1995)
11. L. Mertz: "Concentric spectrographs", *Appl. Opt.* **16**, 3122-3124 (1977)
12. D. Kwo, G. Lawrence, and M. Chrisp: "Design of a grating spectrometer from a 1:1 mirror system", SPIE Proc. **818**, 275-279 (1987)
13. D. R. Lobb: "Theory of concentric designs for grating spectrometers", *Appl. Opt.* **33**, 2648-2658 (1994)
14. F. Reininger, M. Dami, R. Paolinetti, S. Pieri, and S. Falugiani: "Visible infrared mapping spectrometer – visible channel (VIMS-V)", in *Instrumentation in Astronomy VIII*, SPIE Proc. **2198**, 239-250 (1994)
15. F. Reininger and 46 coauthors: "VIRTIS: visible infrared thermal imaging spectrometer for the Rosetta mission", in *Imaging Spectrometry II*, M. R. Descour and J. M. Mooney eds., *Proc. SPIE* **2819**, 66-77 (1996)
16. D. R. Lobb: "Imaging spectrometers using concentric optics", in *Imaging Spectrometry III*, M. R. Descour and S. S. Shen Eds., SPIE Proc. **3118**, 339-347 (1997)
17. M. Chrisp: "Convex diffraction grating imaging spectrometer". U.S. Pat. No. 5,880,834 (1999)
18. P. Mouroulis: "Low distortion imaging spectrometer designs utilizing convex gratings", in *International Optical Design Conference 1998*, SPIE Proc. **3482**, 594-601 (1998)
19. P. Mouroulis, D. W. Wilson, P. D. Maker, and R. E. Muller: "Convex grating types for concentric imaging spectrometers", *Appl. Opt.* **37**, 7200-7208 (1998).

Figure Captions

Figure 1. Schematic of an ideal spectrum produced by a pushbroom imaging spectrometer

Figure 2. Schematic of errors in the spectrum of a non-ideal pushbroom imaging spectrometer

Figure 3: Modeled total, scattered, and reflected upwelling radiance as a function of wavelength, mid-latitude summer atmosphere, 23 km visibility, 0.25 reflectance, sea level, 45° zenith angle.

Figure 4. (a): Compact Offner spectrometer for the 1000-2500 nm range (y-z view). (b): x-z view

Figure 5. Maximum SRF variation for Offner spectrometer 1. The two curves represent SRFs from two different field positions at a single wavelength. The wavelength and field positions were chosen to represent the worst case (maximum difference) for all wavelengths and fields.

Figure 6. Maximum SRF variation for Offner spectrometer 2. In this case, the SRF is nearly invariant with field position for every wavelength.

Figure 7. Maximum spatial response function variation, Offner spectrometer 1. The two curves represent SiRFs for two different wavelengths at a single field position. The wavelengths and field position were chosen to represent the worst case (maximum difference) for all wavelengths and fields.

Figure 8. Maximum spatial response function variation, Offner spectrometer 2.

Figure 9. (a): Compact Dyson spectrometer example, y-z view. An additional small cemented block of fused silica is shown at the input, in order to allow some degrees of freedom for design optimization. A small gap was allowed between the exit flat silica face and the image plane. (b): Dyson spectrometer example, x-z view. The slit and its image are nearly coincident.

Figure 10. Maximum SRF variation, Dyson spectrometer 1.

Figure 11. Maximum SRF variation, Dyson spectrometer 2.

Figure 12. Maximum spatial response function variation, Dyson spectrometer 1.

Figure 13. Maximum spatial response function variation, Dyson spectrometer 2.

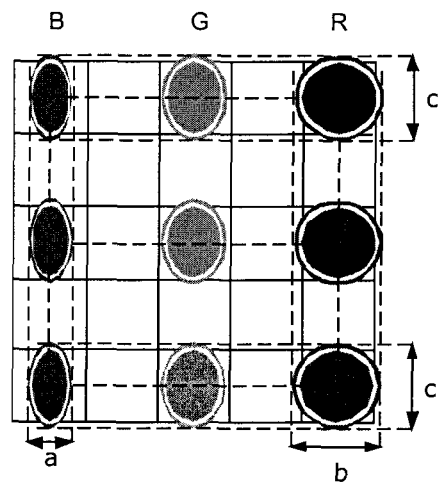


Figure 1

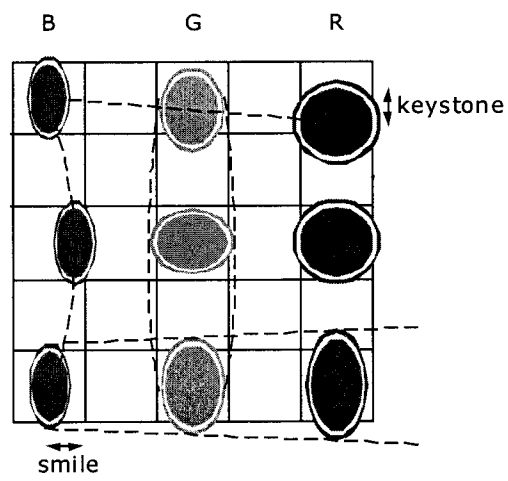


Figure 2

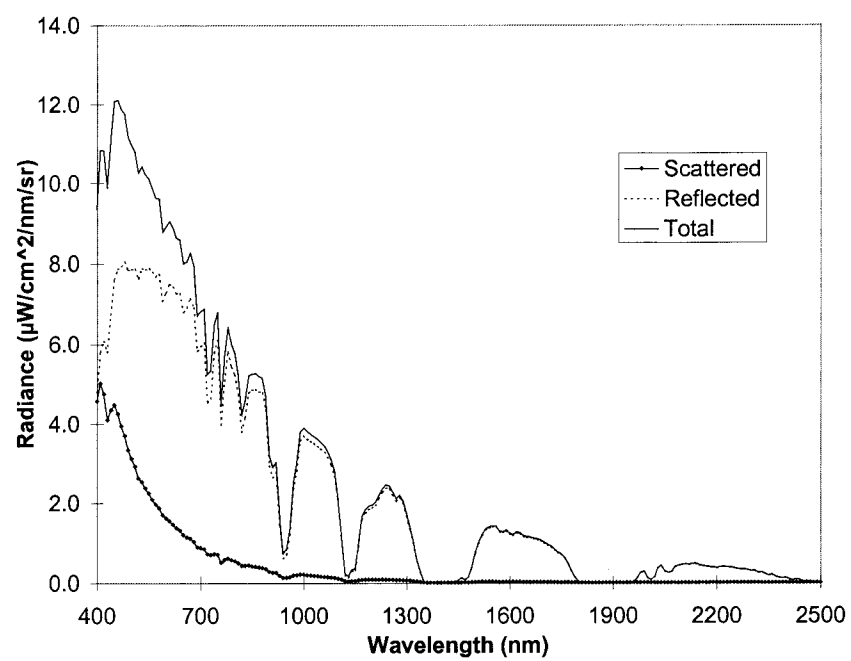


Figure 3

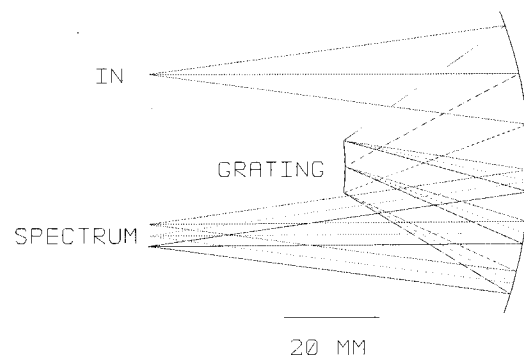


Figure 4(a)

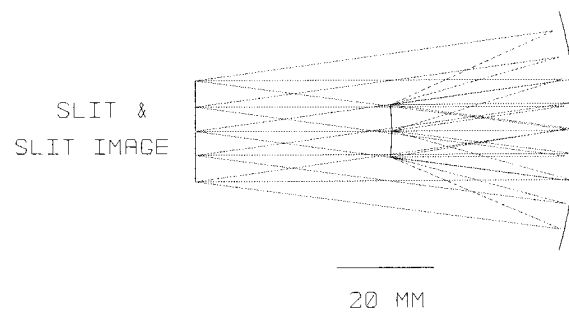


Figure 4(b)

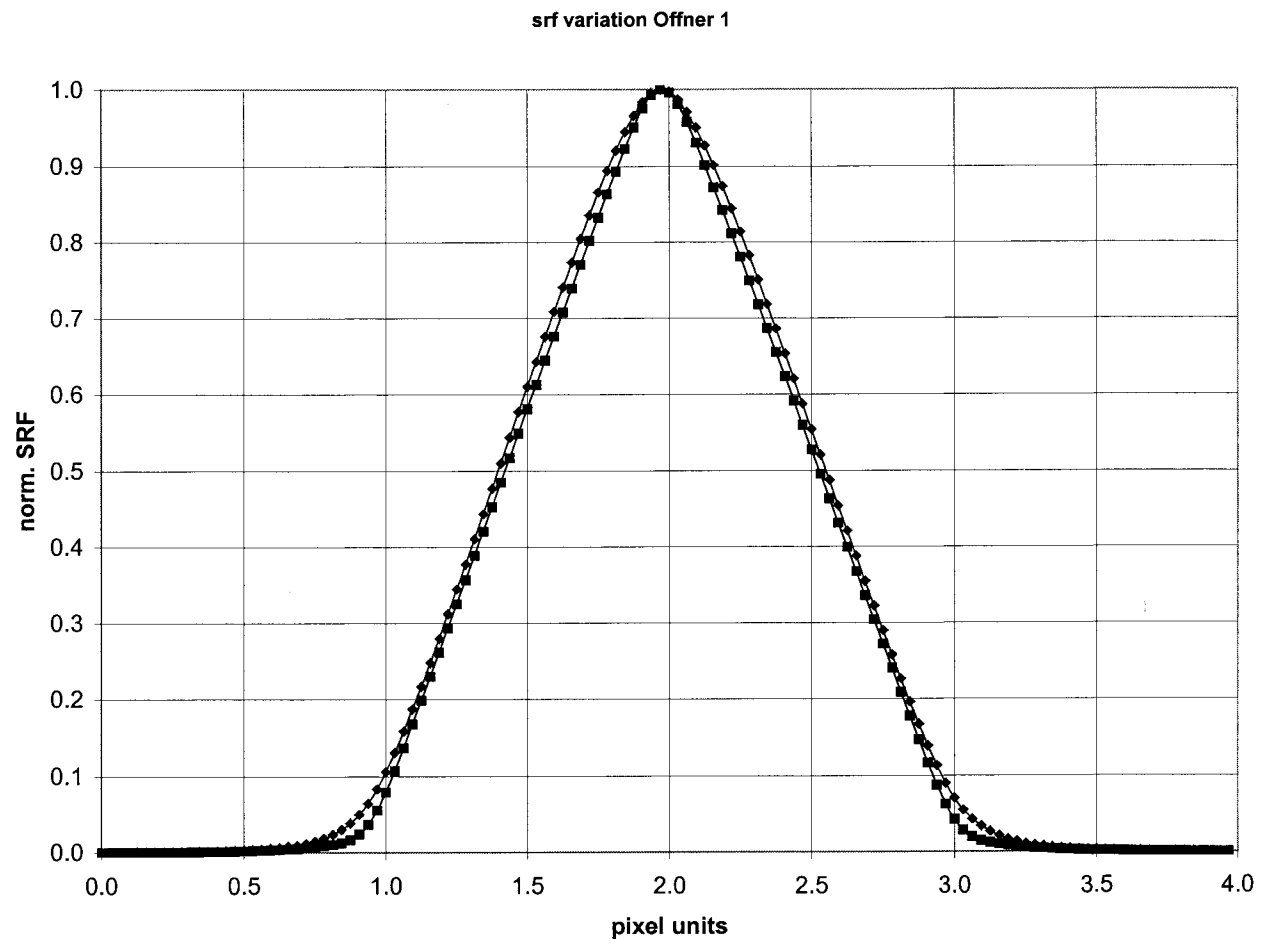


Figure 5

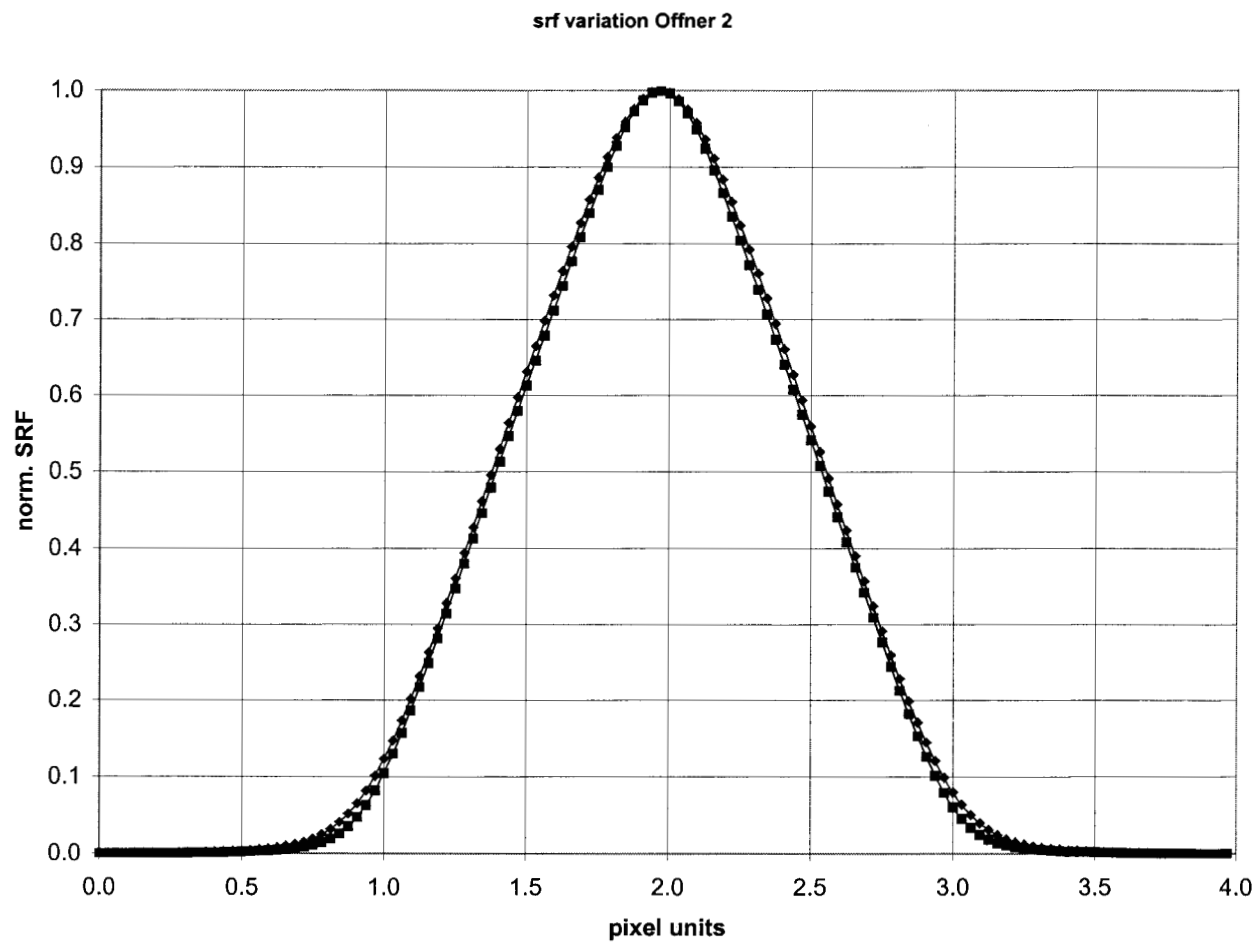


Figure 6

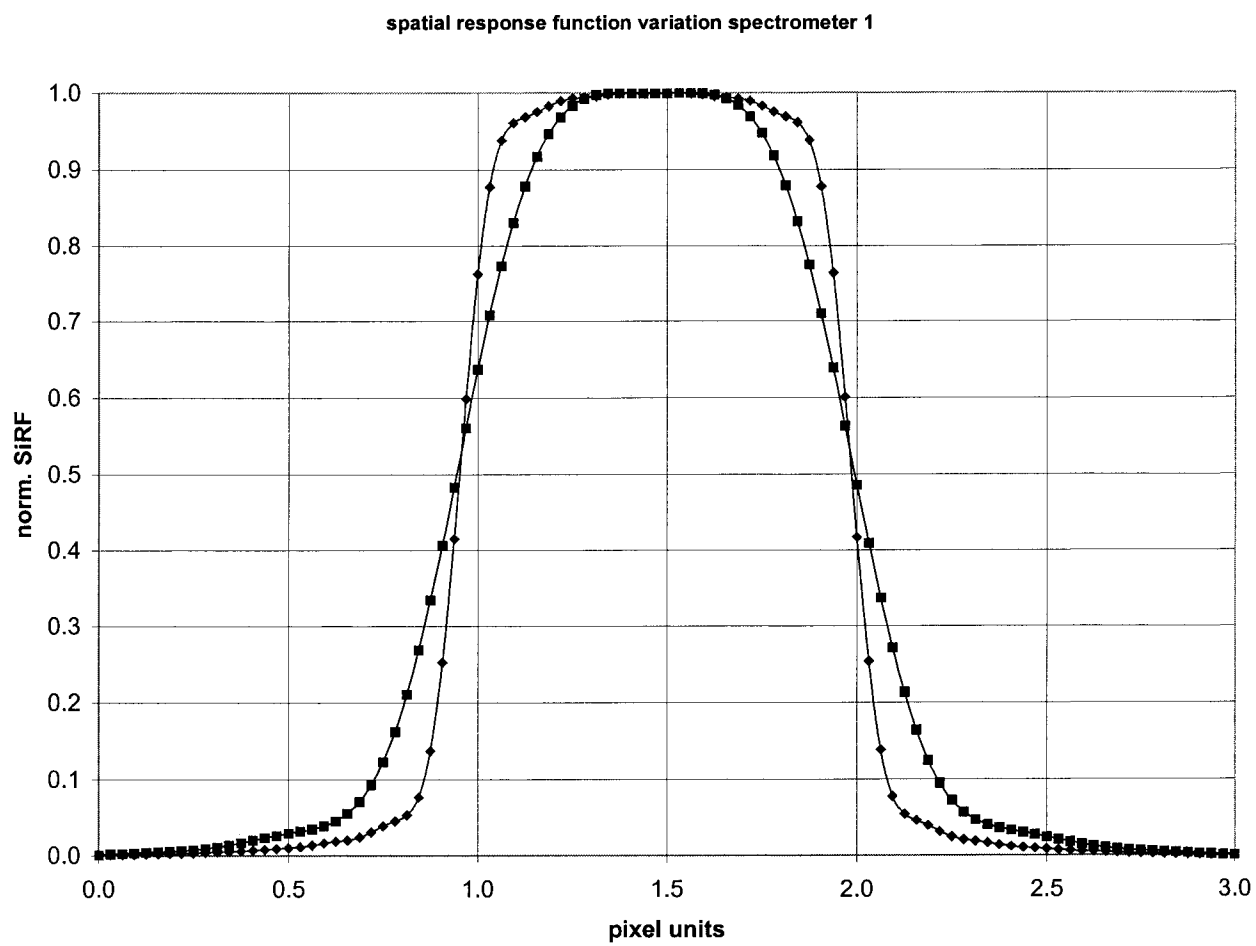


Figure 7

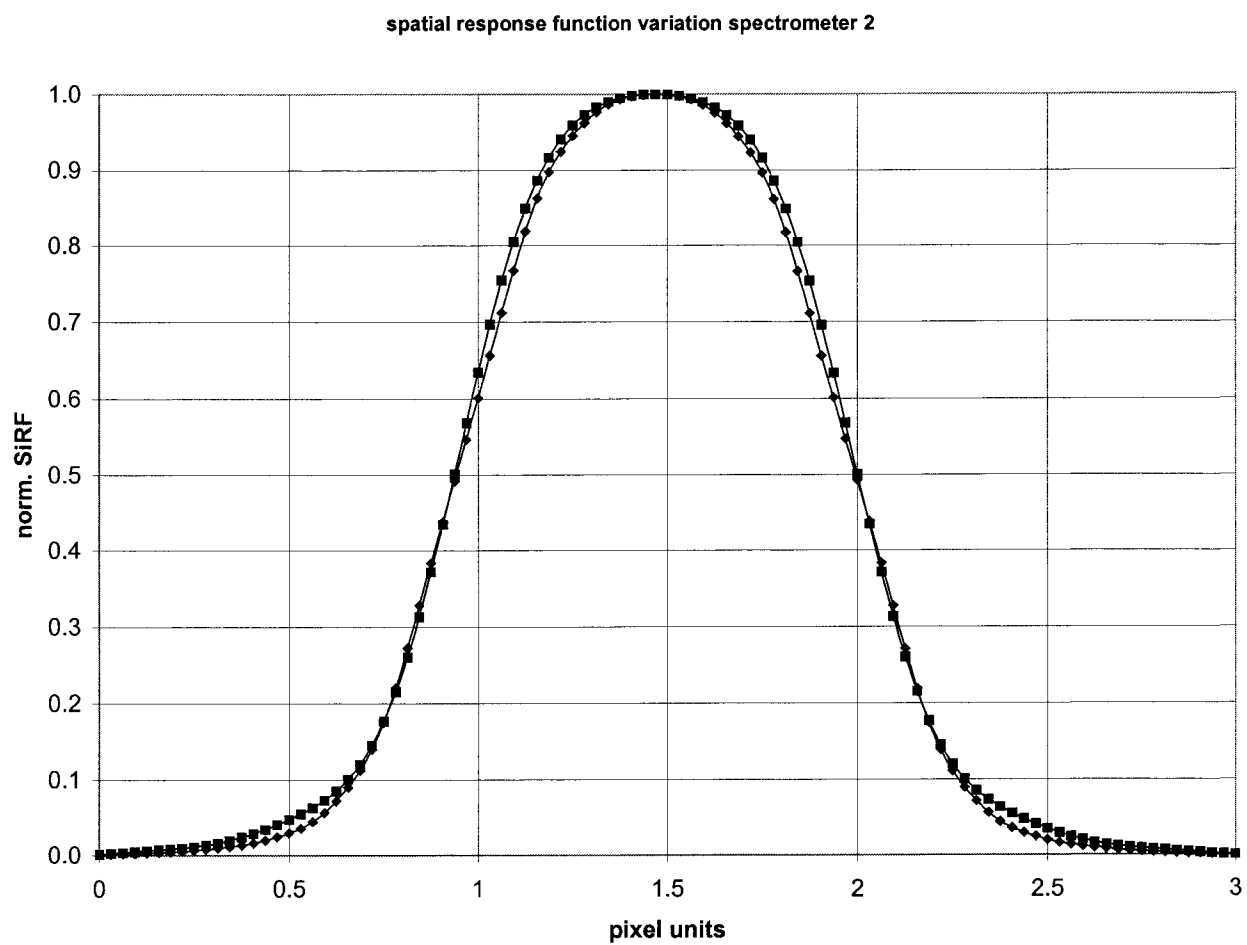


Figure 8

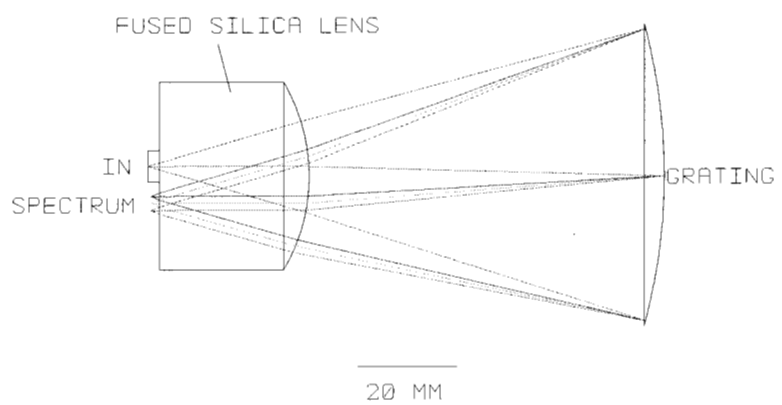


Figure 9 (a)

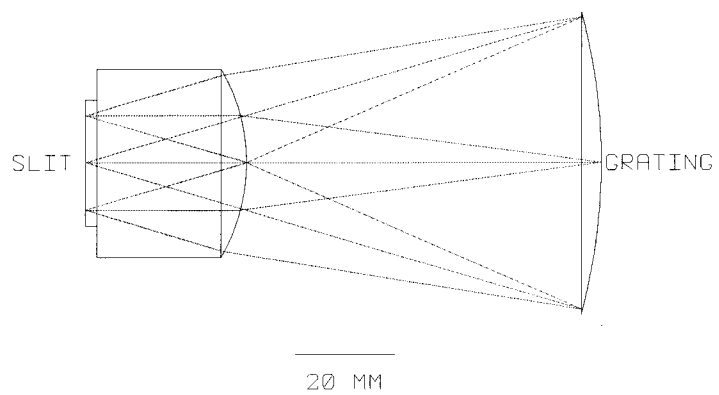


Figure 9 (b)

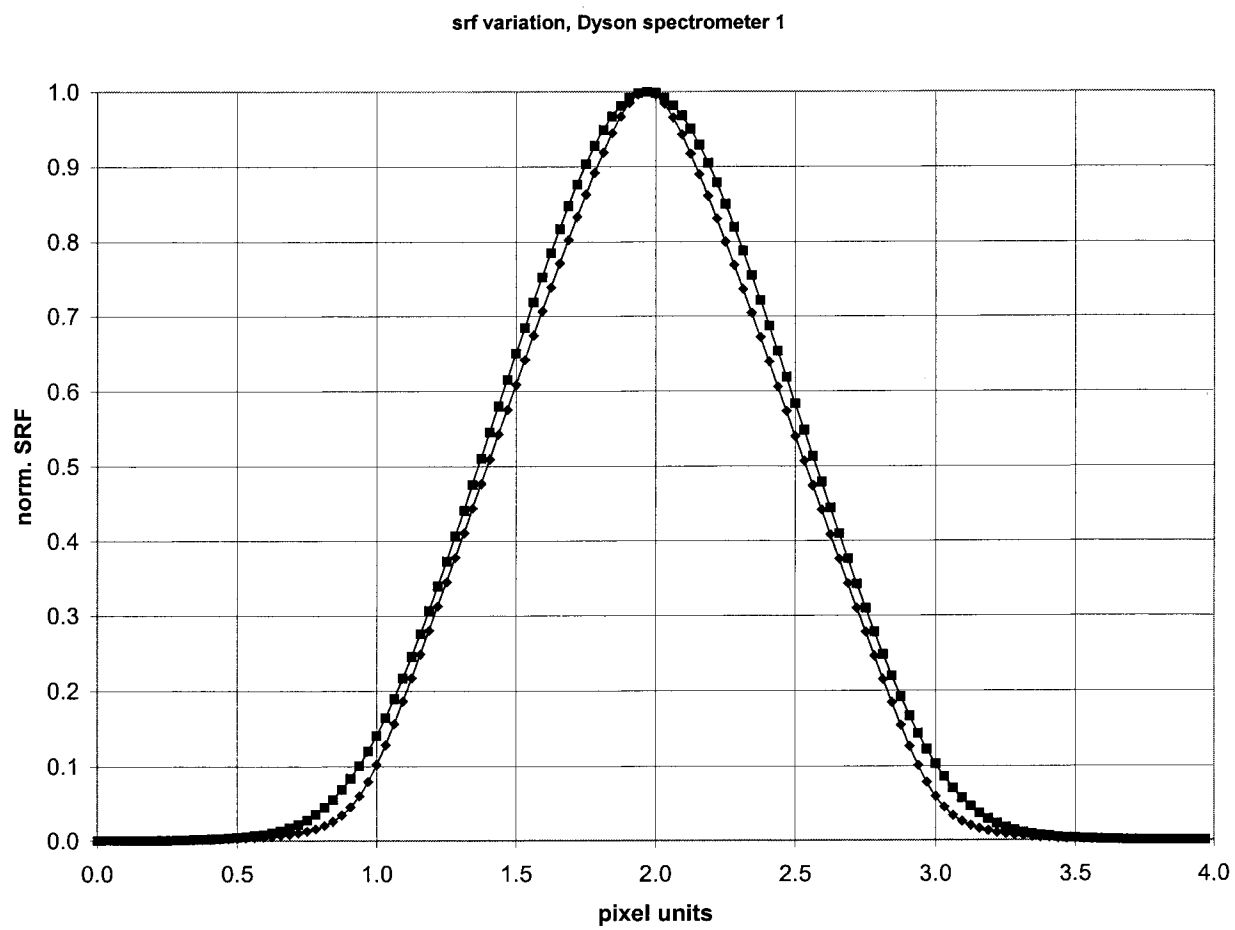


Figure 10

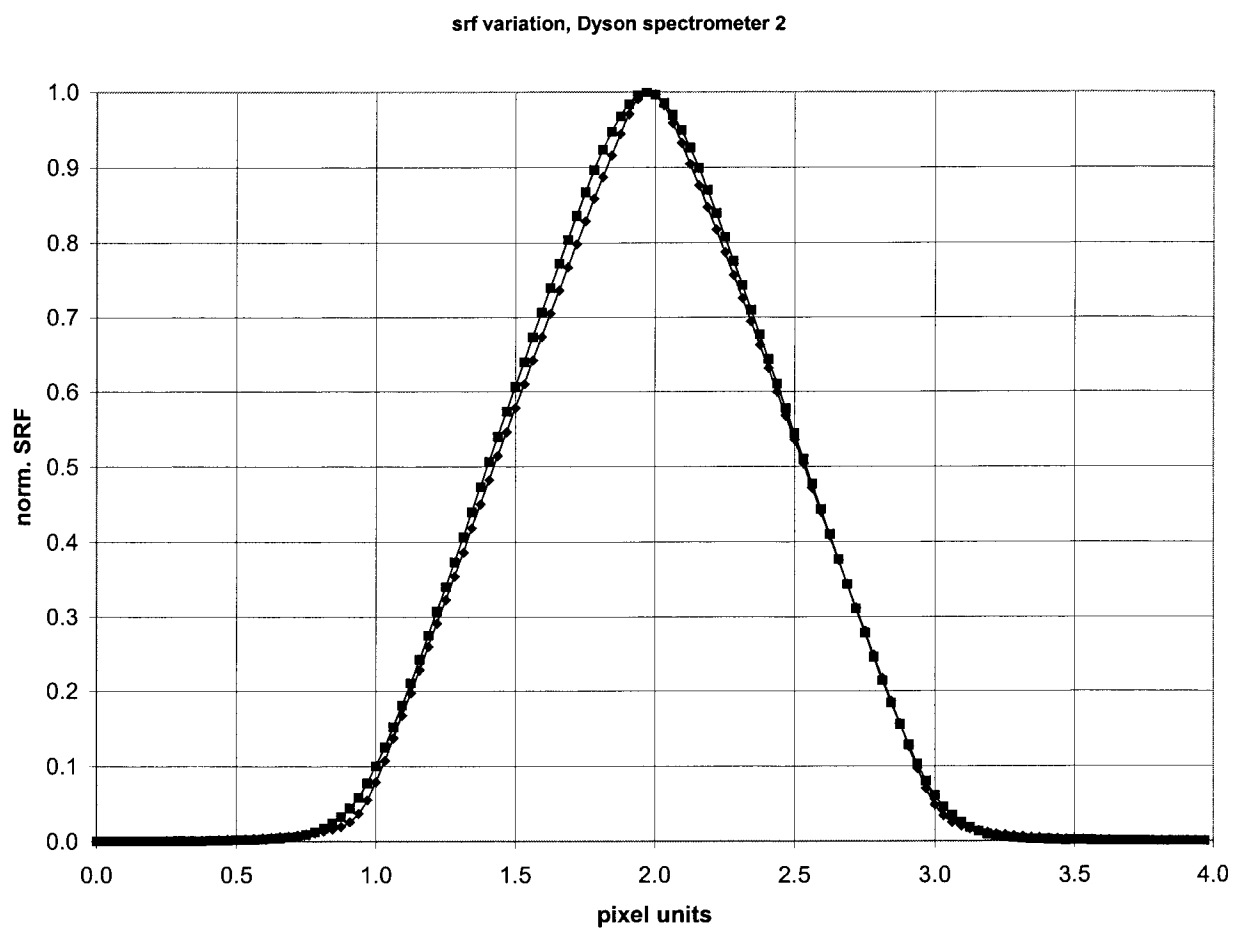


Figure 11

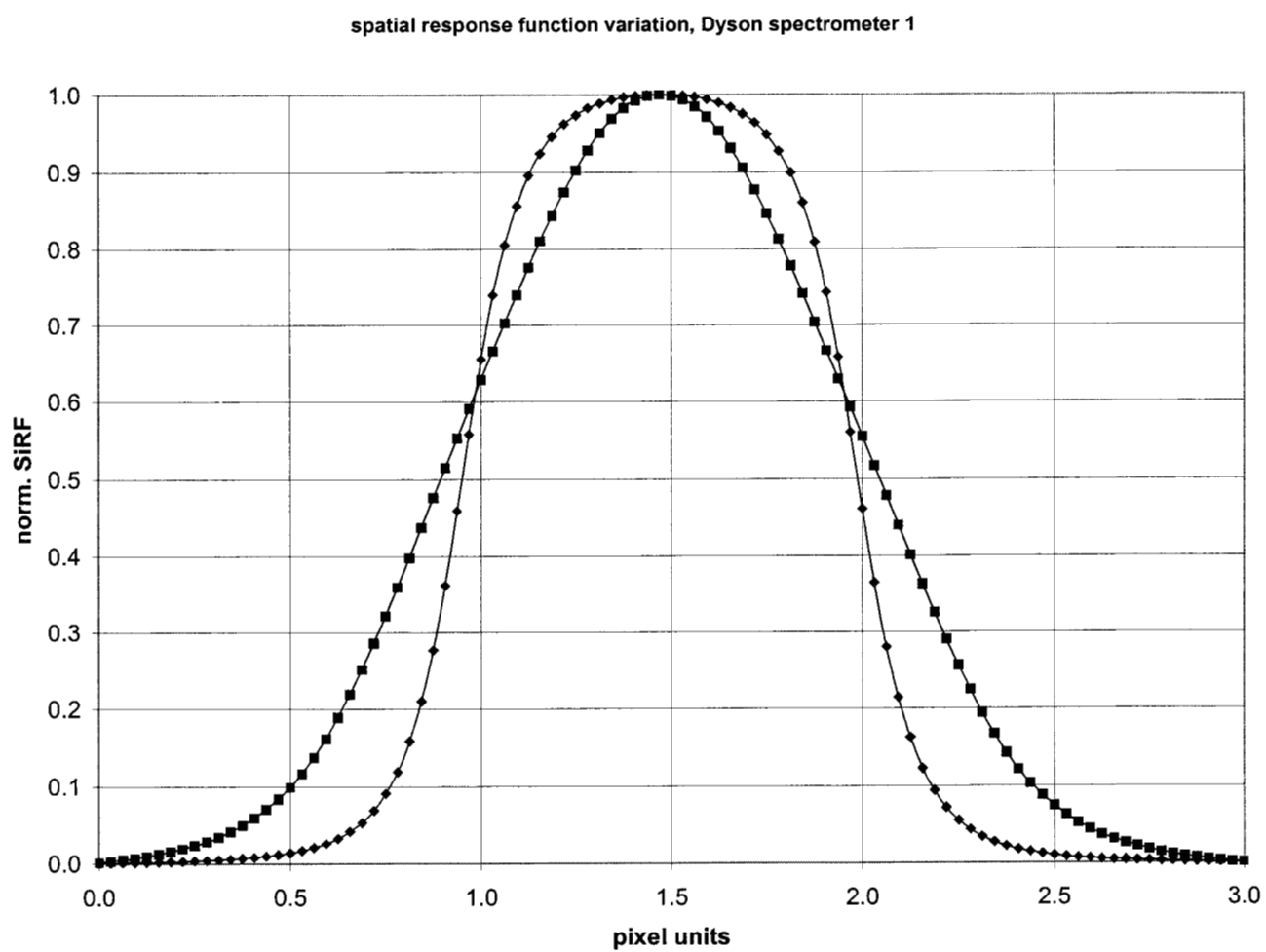


Figure 12

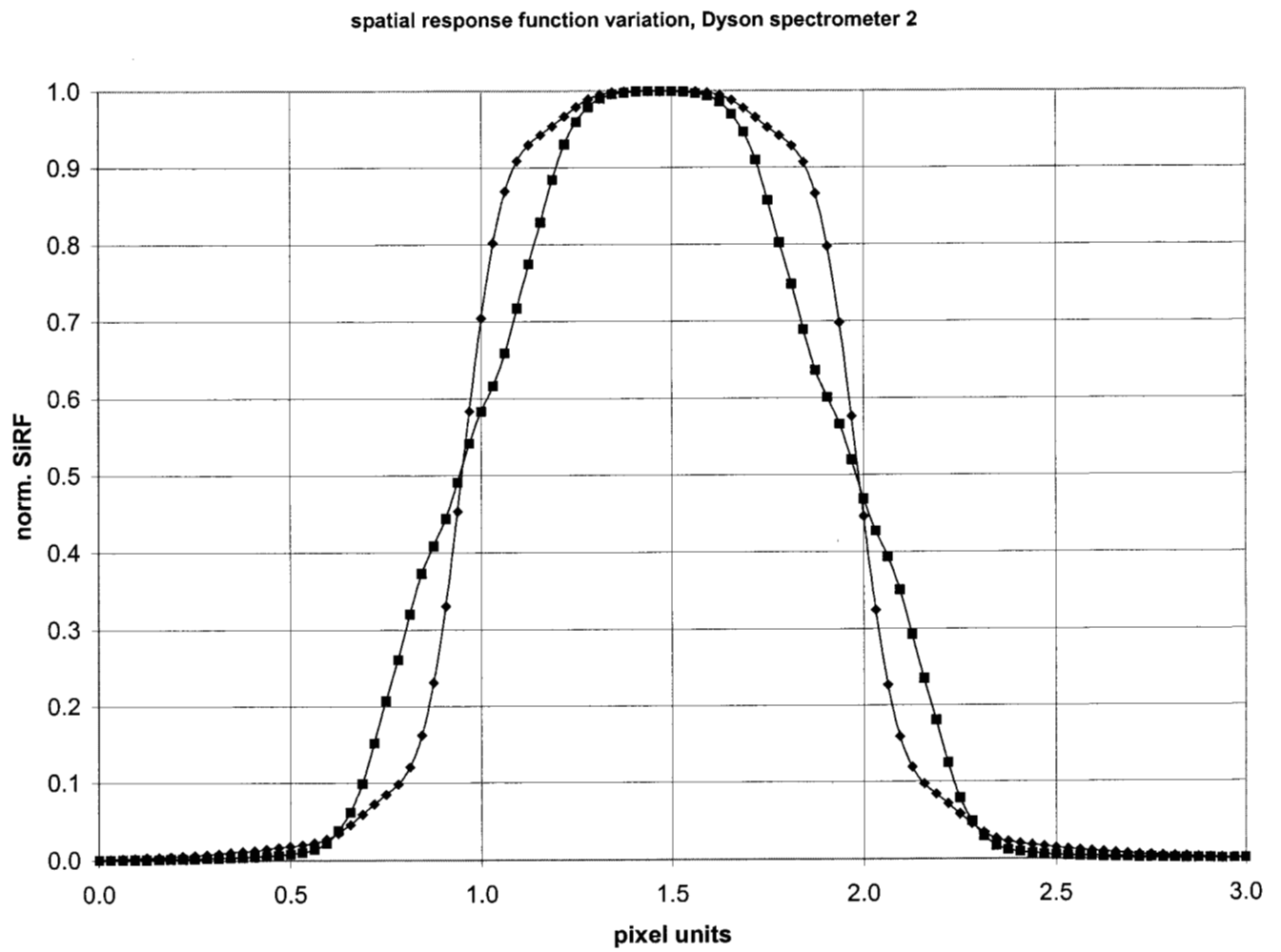


Figure 13